

The pristine dwarf-galaxy survey – III. Revealing the nature of the Milky Way globular cluster Sagittarius II

Nicolas Longeard,^{1★} Nicolas Martin,^{2,3} Rodrigo A. Ibata,² Else Starkenburg,^{4,5} Pascale Jablonka,^{1,6★} David S. Aguado,⁷ Raymond G. Carlberg,⁸ Patrick Côté,⁹ Jonay I. González Hernández,^{10,11} Romain Lucchesi,¹ Khyati Malhan,¹² Julio F. Navarro,¹³ Rubén Sánchez-Janssen,¹⁴ Guillaume F. Thomas,⁹ Kim Venn¹² and Alan W. McConnachie⁹

¹Laboratoire d'astrophysique, École Polytechnique Fédérale de Lausanne (EPFL), Observatoire, CH-1290 Versoix, Switzerland

²Université de Strasbourg, CNRS, Observatoire astronomique de Strasbourg, UMR 7550, F-67000 Strasbourg, France

³Max-Planck-Institut für Astronomie, Königstuhl 17, D-69117 Heidelberg, Germany

⁴Leibniz Institute for Astrophysics Potsdam (AIP), An der Sternwarte 16, D-14482 Potsdam, Germany

⁵Kapteyn Astronomical Institute, University of Groningen, Landleven 12, NL-9747 AD Groningen, the Netherlands

⁶GEPI, Observatoire de Paris, Université PSL, CNRS, Place Jules Janssen, F-92195 Meudon, France

⁷Institute of Astronomy, University of Cambridge, Madingley Road, Cambridge CB3 0HA, UK

⁸Department of Astronomy and Astrophysics, University of Toronto, Toronto, ON M5S 3H4, Canada

⁹NRC Herzberg Astronomy and Astrophysics, 5071 West Saanich Road, Victoria, BC V9E 2E7, Canada

¹⁰Instituto de Astrofísica de Canarias, Vía Láctea, E-38205 La Laguna, Tenerife, Spain

¹¹Universidad de La Laguna, Departamento de Astrofísica, E-38206 La Laguna, Tenerife, Spain

¹²The Oskar Klein Centre for Cosmoparticle Physics, Department of Physics, Stockholm University, AlbaNova, SE-10691 Stockholm, Sweden

¹³University of Victoria, 3800 Finnerty Rd, Victoria, BC V8P 5C2, Canada

¹⁴STFC UK Astronomy Technology Centre, Royal Observatory, Blackford Hill, Edinburgh EH9 3HJ, UK

Accepted 2021 February 11. Received 2021 February 2; in original form 2020 May 12

ABSTRACT

We present a new spectroscopic study of the faint Milky Way satellite Sagittarius II. Using multiobject spectroscopy from the Fibre Large Array Multi-Element Spectrograph, we supplement the data set of Longeard et al. with 47 newly observed stars, 19 of which are identified as members of the satellite. These additional member stars are used to put tighter constraints on the dynamics and the metallicity properties of the system. We find a low velocity dispersion of $\sigma_v^{\text{SgrII}} = 1.7 \pm 0.5 \text{ km s}^{-1}$, in agreement with the dispersion of Milky Way globular clusters of similar luminosity. We confirm the very metal-poor nature of the satellite ($[\text{Fe}/\text{H}]_{\text{spectro}}^{\text{SgrII}} = -2.23 \pm 0.07$) and find that the metallicity dispersion of Sgr II is not resolved, reaching only 0.20 at the 95 per cent confidence limit. No star with a metallicity below -2.5 is confidently detected. Therefore, despite the unusually large size of the system ($r_h = 35.5_{-1.2}^{+1.4} \text{ pc}$), we conclude that Sgr II is an old and metal-poor globular cluster of the Milky Way.

Key words: Globular Clusters: individual: Sagittarius II – Local Group.

1 INTRODUCTION

The faint and metal-poor satellites of massive galaxies are among the oldest structures of the Universe, whether they are dwarf galaxies or globular clusters (White & Rees 1978; Beasley et al. 2002; Mo, van den Bosch & White 2010). Because the faintest, low-mass galaxies are, in a Λ CDM context, dominated by dark matter (DM), they can be the key to constraining the nature of the DM particle and more broadly the properties of our Universe (Klypin et al. 1999; Geringer-Sameth, Koushiappas & Walker 2015; Bullock & Boylan-Kolchin 2017; Nadler et al. 2019). For example, the high mass-to-light ratios of dwarf galaxies make them candidates of choice to detect the particle itself through a self-annihilation process (Geringer-Sameth et al. 2015; Simon et al. 2020). The mass of the DM particle can be

constrained by studying the luminosity function of the known MW dwarf galaxies (Jethwa, Erkal & Belokurov 2018) that, in return, make predictions about the number of future discoveries that will be made by facilities such as the Vera Rubin Observatory given our current understanding of the DM particle. Furthermore, the old age of the dwarf galaxies further implies that they could host Population III stars (Ishiyama et al. 2016) originally formed in DM minihaloes, while their low mass and metallicity suggest that the pollution from successive supernovae is limited in these systems (Dekel & Silk 1986; Frebel & Norris 2015). As a consequence, they are unique laboratories to study and quantify the different evolutionary pathways of stellar formation (Roederer et al. 2016; Webster, Frebel & Bland-Hawthorn 2016; Ji et al. 2019).

On the other hand, globular clusters are not thought to be DM-dominated (Moore 1996 and references therein) and the faintest of them are often modelled as simpler systems with minimal or no detectable metallicity dispersion (Gratton et al. 2007; Carretta

* E-mail: nicolas.longeard@epfl.ch (NL); pascale.jablonka@epfl.ch (PJ)

et al. 2009; Cohen et al. 2010; Willman & Strader 2012). They are important for various reasons. They give us insight in the mode of stellar formation in the early Universe and its similarities and differences with star formation today (Gieles et al. 2018; Gratton et al. 2019). The close link of their properties to those of their host galaxies has become clear over the years: for example, the number of clusters are related to the properties of their host galaxies (Brodie & Huchra 1991; Blakeslee 1997). They are thereby direct probes of their galaxy’ properties and therefore indirect probes for cosmology (Côté, West & Marzke 2002; Villaume et al. 2019; Riley & Strigari 2020). Old globular clusters are also witnesses of the build-up of massive galaxies haloes, which are thought to have formed by disrupting and accreting faint stellar systems (Beasley et al. 2018; Pfeffer et al. 2018). They can also offer a unique insight into the observational validation of stellar population models (Chantereau, Charbonnel & Meynet 2016).

The diversity of the properties of the MW faint satellites has been progressively unveiled over the past decades. Sculptor and Fornax were the first discovered dwarf spheroidal galaxies (Shapley 1938a,b) and the list has only grown longer over the years (Willman et al. 2005; Belokurov et al. 2006; Zucker et al. 2006; Drlica-Wagner et al. 2015; Kim & Jerjen 2015; Laevens et al. 2015; Homma et al. 2016; Torrealba et al. 2018; Homma et al. 2019). Their observed diversity in size, luminosity, and mass naturally arises in various simulations trying to reproduce our Local Universe (Springel et al. 2008; Vogelsberger et al. 2014; Schaye et al. 2015; Wheeler et al. 2019). For the Milky Way’s globular clusters, Harris (2010) has compiled the properties of 157 systems and summarized years of efforts of the community to characterize and understand them. That list will only grow longer in the future considering the recent discoveries of new clusters (Martin et al. 2016c; Koposov, Belokurov & Torrealba 2017; Mau et al. 2019), especially with the advent of the Legacy Survey of Space and Time (LSST) in the incoming years (Ivezić et al. 2008; Simon 2019).

As increasingly faint MW satellites are discovered, the difficulties in classifying them have grown. Systems fainter than $M_V \sim -6$ mag are often challenging to classify as globular clusters or galaxies. This issue was notably addressed by Côté et al. (2002) and Gilmore et al. (2007) and is commonly known as the ‘valley of ambiguity’. Distinguishing faint satellite galaxies from globular clusters relies on two main diagnostics: (i) evidence for the presence of substantial amounts of dark matter, and (ii) the presence of a substantial dispersion in metallicity, a feature usually associated with recurrent star formation. This requires combining deep photometry with extensive spectroscopic campaigns. Dynamical evidence for an excess of mass over that of the stellar component, would then be attributed, in the standard cosmological model, to the presence of a massive DM halo (Willman & Strader 2012) and would favour a dwarf galaxy scenario. The first measurement of the velocity dispersion of a non-classical MW dwarf galaxy, undertaken by Kleyna et al. (2005), showed that Ursa Major I is indeed DM-dominated. This effort was repeated for most systems known at the time, enriching our knowledge of the MW satellites’ properties (Martin et al. 2007; Simon & Geha 2007a; Koposov et al. 2011; Simon et al. 2011; Martin et al. 2016b), an effort that would also rely on other tracers such as the metallicity and the metallicity dispersion of these faint satellites (Kirby et al. 2008; Koposov et al. 2015; Walker et al. 2016). However, in practice, the velocity and metallicity dispersions can be challenging to constrain due to the low number of member stars observed with spectroscopy for a significant fraction of the known faint MW satellites. This problem, that first arose with the study of the kinematics of Segue 2 (Kirby et al. 2013a), still limits our understanding of some of them. The examples over

the last few years are numerous, with Draco II (Martin et al. 2016a; Longeard et al. 2018), Tucana III (Simon et al. 2017), Colomba I or Horologium II (Fritz et al. 2019) that are still not well understood, despite extensive studies with photometry and spectroscopy.

In that context, we present a new spectroscopic study of the faint MW satellite Sagittarius II (Sgr II) discovered by Laevens et al. (2015), and studied in depth by Longeard et al. (2020, L20). L20 used deep photometry, multiobject spectroscopy and the metallicity-sensitive, narrow-band photometry provided by the Pristine survey (Starkenburg et al. 2017) to refine the structural properties of Sgr II and infer its dynamical and metallicity properties for the first time. Its velocity dispersion ($\sigma_{vr}^{L20} = 2.7^{+1.3}_{-1.0} \text{ km s}^{-1}$) favoured the existence of a low-mass DM halo and therefore a dwarf galaxy scenario. The metallicity of the satellite was found to be in good agreement with the metallicity–luminosity relation of dwarf galaxies of Kirby et al. (2013b), while its metallicity dispersion was deemed small ($\sigma_{[Fe/H]}^{L20} = 0.10^{+0.06}_{-0.04}$) but resolved. This last result, however, could be inflated by systematics, an underestimation of the individual uncertainties on the spectroscopic metallicities, or just by the small sample of six stars used to perform the metallicity analysis. L20 marginally favours Sgr II to be a very low-mass galaxy because of two member stars with discrepant metallicity measurements in a very limited-sized sample, with only six stars used to estimate the metallicity dispersion. An independent study of the satellite presented in an American Astronomical Society meeting (Simon et al. 2019), yet to be published, unequivocally found that Sgr II is a globular cluster, based on an extremely low metallicity dispersion measurement from their own spectroscopic sample (<0.08 at the 95 per cent confidence level). For the rest of this paper, the results of L20 will be used. In many ways, Sgr II is shrouded in mystery, and the following work will attempt to close the case on the nature of this faint and elusive satellite.

2 DATA SELECTION AND ACQUISITION

The spectroscopy used in this work is a combination of two data sets. The first data were observed with the DEep Imaging Multi-Object Spectrograph (DEIMOS; Faber et al. 2003), already detailed and analysed in L20. The second data set is composed of new observations performed with the Fibre Large Array Multi-Element Spectrograph (FLAMES; Pasquini et al. 2002) mounted on the Very Large Telescope (VLT). The GIRAFFE/HR21 grating, with a resolution of $R \sim 18000$, a central wavelength of 8757 Å and a bandwidth between 8484 and 9001 Å , was used to resolve the Calcium II triplet infrared lines. These FLAMES observations were conducted during three different nights to attempt to detect binary stars: on the 06/22/2016 ($1 \times 2610 \text{ s}$ of integration), the 07/21/2016 ($2 \times 2610 \text{ s}$), and the 07/30/2016 ($2 \times 2610 \text{ s}$).

The data were reduced by the European Southern Observatory team using their pipeline specifically tailored to FLAMES data (Melo et al. 2009). The spectrum of a Sgr II member star is displayed in Fig. 1 to illustrate the quality of the data. In order to infer the radial velocities, the equivalent widths and their respective uncertainties, the method already used in L20 was used and consists of determining the combination of Gaussian profiles that best fits a continuum composed of the Calcium II triplet lines at rest as the unique spectral features. It also includes a correction to account for the non-Gaussianity of the wings’ lines. The typical uncertainty on the radial velocities for the FLAMES data set is of the order of 1 km s^{-1} , and all the stars with a signal-to-noise (S/N) ratio below 3 per resolution element are discarded from the sample. In the same fashion as in Simon & Geha (2007b) and L20, the systematic error

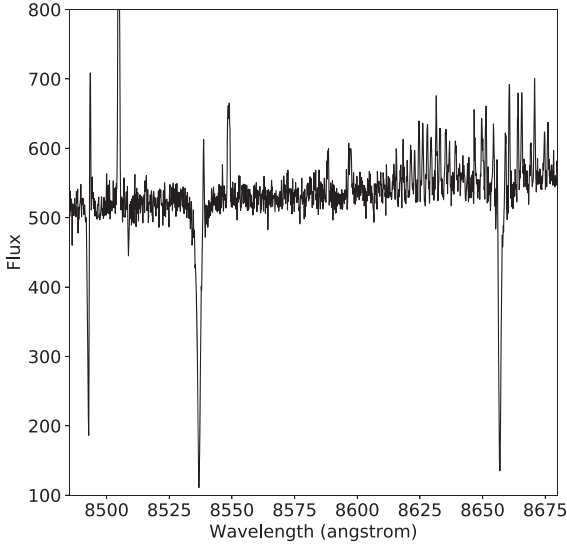


Figure 1. Spectrum of a Sgr II member star with a S/N of ~ 65 focusing on the Calcium II triplet lines. This spectrum is not sky-subtracted in order to give the reader a flavour of the ‘raw’ quality of the data. This star has a metallicity of $[\text{Fe}/\text{H}] = -2.32 \pm 0.18$ using the calibration of Starkenburg et al. (2010) as detailed in Section 3.2.

on the velocities is the residuals of the velocities measured across different epoch and is determined from stars observed more than once in the FLAMES sample. The resulting systematics are a bias with respect to the DEIMOS velocities of $b = 0.4 \pm 0.3 \text{ km s}^{-1}$ and a standard deviation of $\delta_{\text{thr}} = 0.8 \pm 0.1 \text{ km s}^{-1}$.

To build our list of FLAMES targets, we used the locations of stars in the colour–magnitude diagram (CMD) of Sgr II built from deep MegaCam photometry and shown in the right-hand panel of Fig. 2, along with their spatial distribution in the left-hand panel. More importantly, this spectroscopic study benefits from the use of the narrow-band, metallicity-sensitive photometry provided by the Pristine survey (Starkenburg et al. 2017). All stars observed in Pristine have a photometric metallicity measurement, as illustrated in the colour–colour diagram shown in Fig. 3. In this diagram, stars are distributed according to their metallicities, from the most metal-rich at the bottom of the plot, to the most metal-poor at the top, down to a metallicity of $[\text{Fe}/\text{H}] \sim -4.0$. Using the prior knowledge that Sgr II is indeed a very metal-poor satellite ($[\text{Fe}/\text{H}]_{\text{SgrII}} \sim -2.28$, L20), the target list was built so that the stars observed are confirmed to be very metal-poor according to the Pristine survey. In doing so, we increase the probability of finding new members (Youakim et al. 2017; Aguado et al. 2019). The DEIMOS spectroscopy supplementing this data set consists only of the DEIMOS stars identified as non-variables, non-binaries, and metal-poor according to Pristine ($[\text{Fe}/\text{H}]_{\text{CaHK}} < -1.6$) by L20.

In order to clean the FLAMES data, we check for the existence of binaries in the sample. For a given star, each measurement from the k -th epoch is assumed to be reasonably well-described by a Gaussian distribution centred on the radial velocity measurement and a standard deviation corresponding to its uncertainty. Then, the probability that the measurement k is discrepant from that of the same star at another epoch j at the 2σ level is computed. This probability corresponds to the star being variable between epochs k and j . The same procedure is used to compute the probability that each velocity measurement of a given epoch is compatible with all the others within 2σ , i.e. the probability that it is not varying. If the product of

the probabilities representing the hypothesis ‘variable’ is greater than the hypothesis ‘non-variable’, then the star is considered a binary star and discarded from the main sample so that their variability does not affect the dynamical analysis of Sgr II. We find a total of six potential binaries in the sample, however, none have the right velocity to be a member of Sgr II.

The final spectroscopic sample consists of 113 stars, with 47 new stars observed with FLAMES as detailed in Table 1 with four stars out of those 47 in common with L20’s sample. As a consistency check, we compare the velocities obtained with FLAMES and DEIMOS for these four stars. The FLAMES and DEIMOS velocities of three out of those four stars are compatible within 1σ . For the fourth one, the velocities agree within 1.2σ .

3 RESULTS: DYNAMICAL PROPERTIES

In this section, we constrain the systemic heliocentric velocity of Sgr II and its associated velocity dispersion.

All stars in our spectroscopic sample with a heliocentric velocity are shown in Fig. 4. As already detailed in Section 2, the final sample consists of all non-binary, non-HB stars compatible with Sgr II’s sequence in the CMD and that appear as very metal-poor using the CaHK photometry. Stars with mediocre CaHK photometry ($\delta_{\text{CaHK}} > 0.1$) from the DEIMOS catalogue are also included as their photometric metallicities are not reliable. Thanks to the photometry provided by the Pristine survey, the FLAMES data are already quite clean with only a few clear contaminants discrepant from the Sgr II population at around -180 km s^{-1} . When available, the proper motions (PMs) provided by the *Gaia* Data Release 2 (*Gaia* Collaboration 2018) are also used to filter out contaminants. This procedure allows us to get rid of one star ($\alpha = 298.084146^\circ$, $\delta = -21.966605^\circ$, $v = -181.7 \pm 0.4 \text{ km s}^{-1}$) with CMD and metallicity properties strongly compatible with Sgr II, but a PM unequivocally discrepant from that of the satellite (Massari & Helmi 2018, L20).

In order to derive the systemic velocity ($\langle v_{\text{SgrII}} \rangle$) and intrinsic velocity dispersion σ_v^{SgrII} of Sgr II, the velocity distribution of our data set and shown in Fig. 4 is assumed to be the sum of two Gaussian distributions, one standing for Sgr II’s population and the other for the MW contamination. The corresponding likelihood for the k -th star in the spectroscopic sample can be written as follows:

$$\begin{aligned} \mathcal{L}(\langle v_{\text{SgrII}} \rangle, \sigma_v^1, \langle v_{\text{MW}} \rangle, \sigma_v^2 | \{v_{r,k}, \delta_{v,k}\}) \\ = \Pi_k (\eta_{\text{SgrII}} \mathcal{G}(\{v_{r,k}, \delta_{v,k}\} | \langle v_{\text{SgrII}} \rangle, \sigma_v^1) \\ - (1 - \eta_{\text{SgrII}}) \mathcal{G}(\{v_{r,k}, \delta_{v,k}\} | \langle v_{\text{MW}} \rangle, \sigma_v^2)), \end{aligned} \quad (1)$$

with $\sigma_v^1 = \sqrt{(\sigma_v^{\text{SgrII}})^2 + \delta_{v,k}^2 + \delta_{\text{thr}}^2}$ (respectively for σ_v^2 for the MW component) where $\delta_{v,k}$ is the individual velocity uncertainty on the k -th star and δ_{thr} the systematic uncertainty determined in Section 2.

The favoured dynamical model is obtained through a Monte Carlo Markov Chain (MCMC; Hastings 1970) algorithm. The Probability Distribution Functions (PDFs) of the systemic heliocentric velocity and the velocity dispersion of Sgr II are displayed in the top panels of Fig. 5. The resulting systemic velocity ($\langle v_{\text{SgrII}} \rangle$) is $-177.2_{-0.6}^{+0.5} \text{ km s}^{-1}$ and is perfectly compatible with the one of L20. The velocity dispersion found in this work is also compatible with L20 ($\sigma_v^{\text{SgrII}} = 2.7_{-1.0}^{+1.3} \text{ km s}^{-1}$), but with much tighter constraints, it is measured to be $\sigma_v^{\text{SgrII}} = 1.7 \pm 0.5 \text{ km s}^{-1}$. Using the formalism of Wolf et al. (2010) which assumes dynamical equilibrium and a flat velocity dispersion profile, this results into a mass-to-light (M/L) ratio of $3.5_{-1.6}^{+2.7} M_\odot L_\odot^{-1}$. Sgr II shows no sign of a velocity dispersion gradient as the determination of its dynamical properties by selecting stars inside and outside 1 arcmin yields no statistical difference. Using the

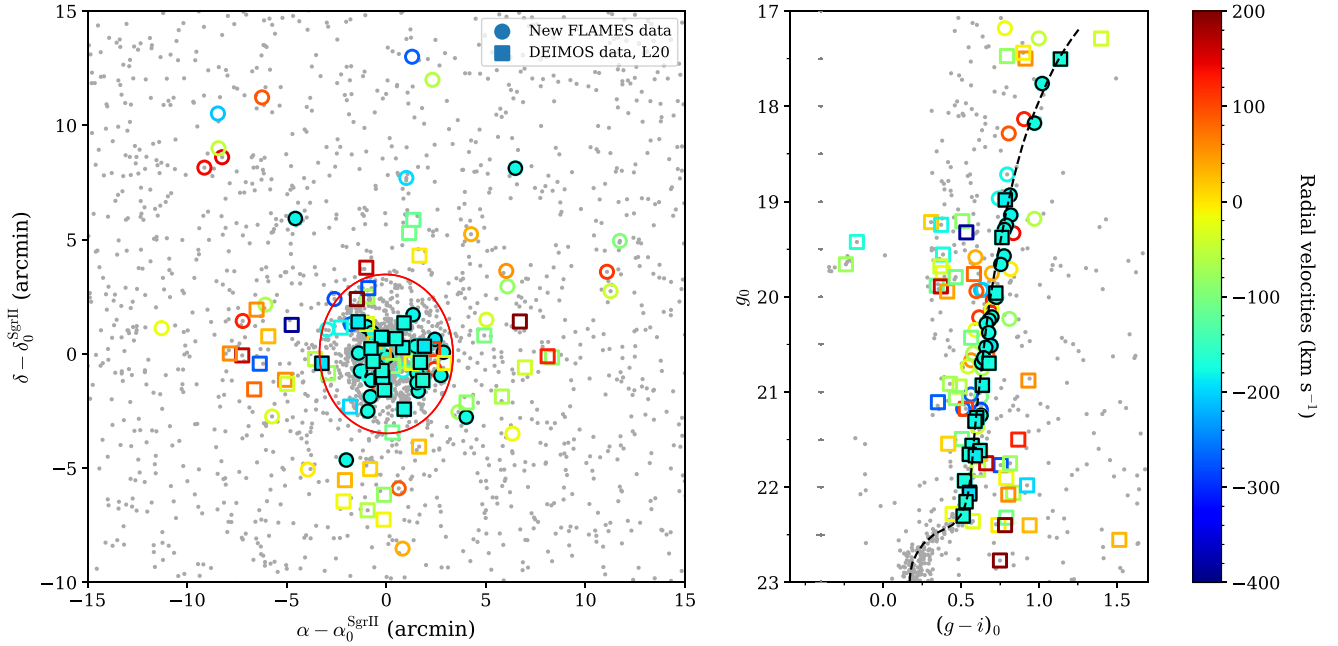


Figure 2. Left-hand panel: Spatial distribution of Sgr II-like stars, i.e. stars with a CMD probability membership of 1 per cent or higher. The field is centred on $(\alpha_0 = 298.16628^\circ, \delta_0 = -22.89633^\circ)$. The red contour defines two half-light radii ($r_h \sim 1.7$ arcmin) of the satellite, as inferred by L20. The locations of all stars in the spectroscopic data set are indicated as large, coloured markers. The squares represent the DEIMOS observations from L20, while the circles stand for the new FLAMES data presented in this work. All stars observed spectroscopically are colour-coded according to their heliocentric velocities. Cyan stars are Sgr II member stars (i.e. dynamical and CMD probabilities above 50 per cent, see Section 3 for more details), and have a radial velocity around -177 km s^{-1} . The filled squares and circles are the member stars of the satellite. Right-hand panel: CMD of Sgr II within two half-light radii (grey) superimposed with the entire spectroscopic data set. The best-fitting Dartmouth isochrone from L20 (12 Gyr, $[\text{Fe}/\text{H}] = -2.35$, $[\alpha/\text{Fe}] = 0$, $m - M = 19.32$ mag) is shown as a black dashed line and is perfectly compatible with the identified members of Sgr II.

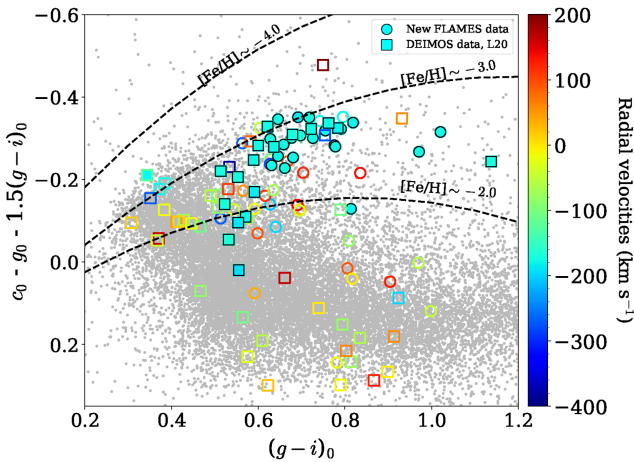


Figure 3. Pristine colour-colour diagram of Sgr II showing field stars (grey) and the spectroscopic data set with large, coloured markers. Member stars of Sgr II are shown with filled markers. While the x-axis is a temperature proxy, the y-axis contains the Pristine metallicity-sensitive, narrow-band photometry denoted c_0 , and therefore the metallicity information. As a result, stars are distributed according to their metallicity: the ones around solar metallicity form the stellar locus where most of the grey field stars are located. As a star goes upwards in the diagram (i.e. lower y-axis value) for a fixed temperature, its metallicity decreases. This is represented more visually with the three isometallicity sequences in black dashed lines, showing where stars with a $[\text{Fe}/\text{H}]$ of -4.0 , -3.0 , and -2.0 should be located. This plot shows the efficiency of Pristine in identifying Sgr II members, as almost all DEIMOS stars dynamically compatible with the satellite come out as metal-poor.

formalism of Martin & Jin (2010), we do not detect any systemic velocity gradient ($dv/dx = 1.1^{+11.7}_{-12.3} \text{ km s}^{-1} \text{ arcmin}^{-1}$). Furthermore, modelling the MW contamination with two normally distributed populations instead of one to account for the dynamical differences between the MW halo and disc stars does not change our results.

We classify as a member of Sgr II any star with line-of-sight velocity and (PM) membership probabilities (when available) above 50 per cent. The PM membership probabilities are computed by using the results of L20 that derive the 2D Gaussian distribution (respectively for the local MW contamination) that best describes the Sgr II population in the PM space. From this model, a PM membership probability can be computed for any star with a PM measurement in the *Gaia* DR2. We identify 22 member stars in the FLAMES data. Three of them were already identified in the L20 data set, leading to the identification of 19 new members. Combined with the spectroscopically confirmed members of L20, 43 stars are confirmed to belong to Sgr II, including binaries and horizontal branch (HB) stars. This underlines the importance of the Pristine photometry. To estimate the success rate of the FLAMES data in identifying new members, we do not simply take the fraction of confirmed members over the overall number of stars observed since the sample of Sgr II candidates identified before observation was not large enough to fill all the FLAMES fibres. Among the 47 new stars observed, only 32 were considered as promising Sgr II candidates. Therefore, it yields a success rate of ~ 60 per cent for the FLAMES data sample based on the Pristine selection. In comparison, the DEIMOS data set of L20, solely based on a CMD-based selection, had a 20 per cent success rate. The contrast is even more striking when considering that the DEIMOS selection focuses on the central

Table 1. Properties of the new FLAMES spectroscopic sample. The Pristine metallicity of a given star is indicated only if $[\text{Fe}/\text{H}]_{\text{CaHK}} < -1.0$. The individual spectroscopic metallicity is reported for stars with $\text{S/N} > 12$ and $g_0 < 20.5$ mag. The bias and systematic threshold δ_{hr} determined in Section 2 is not included in the velocity uncertainties presented in this table.

RA (deg)	DEC (deg)	g_0	i_0	CaHK_0	v_r (km s $^{-1}$)	μ_α^* (mas yr $^{-1}$)	μ_δ (mas yr $^{-1}$)	S/N	$[\text{Fe}/\text{H}]_{\text{CaHK}}$	$[\text{Fe}/\text{H}]_{\text{S10 spectro}}$	Member
298.37718	-21.98293	21.05 \pm 0.01	20.42 \pm 0.01	21.74 \pm 0.04	-96.5 \pm 1.4	5.0 \pm 4.0	-5.1 \pm 2.1	3.5	-2.50 \pm 0.12	-	N
298.28281	-21.92996	19.57 \pm 0.01	18.80 \pm 0.01	20.45 \pm 0.02	-177.8 \pm 0.6	-0.2 \pm 0.5	-1.1 \pm 0.3	24.4	-2.58 \pm 0.12	-2.2 \pm 0.11	Y
298.24280	-21.97804	19.75 \pm 0.01	19.05 \pm 0.01	20.67 \pm 0.02	34.1 \pm 2.4	-1.9 \pm 2.7	-1.9 \pm 1.3	12.7	-1.90 \pm 0.12	-1.5 \pm 0.21	N
298.20794	-21.86545	19.18 \pm 0.01	18.21 \pm 0.01	20.64 \pm 0.02	-58.3 \pm 0.5	-0.6 \pm 0.2	-1.0 \pm 0.1	48.9	-1.25 \pm 0.12	-1.26 \pm 0.16	N
298.18438	-21.93702	19.93 \pm 0.01	19.29 \pm 0.01	20.80 \pm 0.02	-195.5 \pm 3.3	-	-	6.3	-1.72 \pm 0.12	-	N
298.18958	-21.84866	21.18 \pm 0.01	20.66 \pm 0.01	21.84 \pm 0.04	-268.8 \pm 16.9	1.7 \pm 0.2	-2.0 \pm 0.1	3.1	-2.01 \pm 0.12	-	N
298.05410	-21.87831	18.29 \pm 0.01	17.48 \pm 0.01	19.51 \pm 0.01	91.0 \pm 0.3	-	-	79.8	-1.34 \pm 0.12	-1.43 \pm 0.16	N
298.08415	-21.96661	18.93 \pm 0.01	18.12 \pm 0.01	20.03 \pm 0.01	-181.7 \pm 0.4	-12.8 \pm 0.7	-18.6 \pm 0.4	60.6	-1.99 \pm 0.12	-1.8 \pm 0.13	N
298.00202	-21.92952	19.33 \pm 0.01	18.50 \pm 0.01	20.37 \pm 0.02	139.8 \pm 0.4	-	-	31.3	-2.28 \pm 0.12	-2.12 \pm 0.11	N
298.01422	-21.89008	19.93 \pm 0.01	19.30 \pm 0.01	20.73 \pm 0.02	-208.9 \pm 1.0	-4.7 \pm 0.2	-6.0 \pm 0.1	16.4	-2.00 \pm 0.12	-2.24 \pm 0.09	N
298.01803	-21.92193	20.17 \pm 0.01	19.47 \pm 0.01	21.06 \pm 0.03	145.7 \pm 0.9	4.2 \pm 1.2	-6.5 \pm 0.9	14.6	-1.95 \pm 0.12	-1.13 \pm 0.22	N
298.36550	-22.00547	20.22 \pm 0.01	19.60 \pm 0.01	20.98 \pm 0.02	112.9 \pm 2.1	-0.6 \pm 0.6	-1.4 \pm 0.4	15.3	-2.10 \pm 0.12	-2.36 \pm 0.12	N
298.36878	-22.01959	21.36 \pm 0.01	20.76 \pm 0.01	21.95 \pm 0.04	-43.6 \pm 3.0	4.8 \pm 3.1	2.9 \pm 1.8	3.6	-3.11 \pm 0.12	-	N
298.27562	-22.01614	20.23 \pm 0.01	19.42 \pm 0.01	21.40 \pm 0.03	-82.3 \pm 2.8	-0.6 \pm 1.3	-11.3 \pm 0.8	4.1	-1.58 \pm 0.12	-	N
298.27457	-22.00481	20.67 \pm 0.01	20.10 \pm 0.01	21.34 \pm 0.03	54.2 \pm 1.5	-	-	10.1	-2.23 \pm 0.12	-	N
298.23845	-22.11143	20.69 \pm 0.01	20.06 \pm 0.01	21.40 \pm 0.03	-175.5 \pm 0.9	-0.6 \pm 1.3	-0.0 \pm 0.8	10.8	-2.41 \pm 0.12	-	Y
298.25661	-22.0404	20.73 \pm 0.01	20.19 \pm 0.01	21.42 \pm 0.03	-34.7 \pm 1.4	0.4 \pm 1.1	0.0 \pm 0.7	6.1	-2.03 \pm 0.12	-	N
298.23141	-22.10773	20.75 \pm 0.01	20.12 \pm 0.01	21.53 \pm 0.03	-69.0 \pm 1.7	-1.1 \pm 1.1	-1.8 \pm 0.6	4.4	-2.13 \pm 0.12	-	N
298.19512	-22.09244	18.18 \pm 0.01	17.21 \pm 0.01	19.37 \pm 0.01	-175.9 \pm 0.3	-13.5 \pm 0.6	-25.9 \pm 0.4	95.7	-2.31 \pm 0.12	-2.15 \pm 0.12	Y
298.18145	-22.07735	18.72 \pm 0.01	17.92 \pm 0.01	19.56 \pm 0.01	-177.7 \pm 0.8	-7.7 \pm 1.3	-9.1 \pm 0.7	18.3	-2.97 \pm 0.12	-2.18 \pm 0.11	N
298.11270	-22.04758	18.97 \pm 0.01	18.23 \pm 0.01	19.74 \pm 0.01	-178.0 \pm 0.9	-1.3 \pm 1.1	-8.7 \pm 0.6	11.9	-2.91 \pm 0.12	-2.13 \pm 0.18	N
298.19043	-22.03676	19.14 \pm 0.01	18.32 \pm 0.01	20.03 \pm 0.01	-180.2 \pm 0.3	-1.7 \pm 1.5	-1.9 \pm 0.9	53.5	-2.87 \pm 0.12	-2.23 \pm 0.11	Y
298.15270	-22.08463	19.25 \pm 0.01	18.46 \pm 0.01	20.11 \pm 0.01	-176.2 \pm 0.5	12.3 \pm 0.5	-27.2 \pm 0.3	27.6	-2.83 \pm 0.12	-2.23 \pm 0.11	Y
298.15185	-22.09654	19.29 \pm 0.01	18.52 \pm 0.01	20.18 \pm 0.01	-177.6 \pm 0.4	6.8 \pm 3.3	0.1 \pm 2.1	29.0	-2.56 \pm 0.12	-2.25 \pm 0.12	Y
298.18099	-22.20728	19.58 \pm 0.01	18.99 \pm 0.01	20.55 \pm 0.02	35.3 \pm 0.8	-	-	11.7	-1.14 \pm 0.12	-	N
298.21784	-22.06409	19.66 \pm 0.01	18.90 \pm 0.01	20.47 \pm 0.02	-175.1 \pm 0.4	-2.4 \pm 0.7	-5.2 \pm 0.4	34.3	-99.0 \pm 0.00	-2.36 \pm 0.1	Y
298.16019	-22.09027	19.94 \pm 0.01	19.34 \pm 0.01	20.77 \pm 0.02	93.9 \pm 2.8	-0.3 \pm 0.8	-1.3 \pm 0.4	3.6	-1.70 \pm 0.12	-	N
298.19280	-22.05979	19.99 \pm 0.01	19.28 \pm 0.01	20.72 \pm 0.02	-174.3 \pm 0.6	-0.8 \pm 0.3	-1.0 \pm 0.1	22.6	-3.07 \pm 0.12	-2.3 \pm 0.11	Y
298.19388	-22.07918	20.01 \pm 0.01	19.28 \pm 0.01	20.79 \pm 0.02	-176.2 \pm 0.6	-7.1 \pm 1.0	-8.9 \pm 0.6	17.7	-2.67 \pm 0.12	-2.15 \pm 0.13	Y
298.20960	-22.07638	20.03 \pm 0.01	19.33 \pm 0.01	20.87 \pm 0.02	121.4 \pm 1.3	0.0 \pm 0.5	-0.4 \pm 0.3	22.5	-2.26 \pm 0.12	-1.78 \pm 0.13	N
298.16641	-22.06769	20.21 \pm 0.01	19.51 \pm 0.01	20.95 \pm 0.02	-172.2 \pm 1.5	-3.2 \pm 0.6	-4.5 \pm 0.3	10.8	-2.73 \pm 0.12	-2.72 \pm 0.1	Y
298.13014	-22.14273	20.24 \pm 0.01	19.56 \pm 0.01	21.01 \pm 0.02	-178.5 \pm 1.0	-	-	14.5	-2.40 \pm 0.12	-2.06 \pm 0.14	Y
298.14121	-22.06475	20.28 \pm 0.01	19.62 \pm 0.01	21.05 \pm 0.02	-175.2 \pm 1.2	-14.8 \pm 1.5	-20.4 \pm 0.8	15.1	-99.0 \pm 0.00	-1.89 \pm 0.16	Y
298.19401	-22.08638	20.38 \pm 0.01	19.70 \pm 0.01	21.09 \pm 0.03	-175.7 \pm 1.2	-1.2 \pm 0.9	-1.1 \pm 0.5	7.7	-2.78 \pm 0.12	-2.17 \pm 0.11	Y
298.21019	-22.05475	20.51 \pm 0.01	19.82 \pm 0.01	21.20 \pm 0.03	-188.7 \pm 5.8	-1.5 \pm 0.5	-0.8 \pm 0.3	3.8	-3.06 \pm 0.12	-	Y
298.14290	-22.07784	20.53 \pm 0.01	19.87 \pm 0.01	21.23 \pm 0.03	-177.4 \pm 1.3	-1.4 \pm 1.5	-9.8 \pm 0.7	14.3	-2.68 \pm 0.12	-	Y
298.17751	-22.16337	20.60 \pm 0.01	19.93 \pm 0.01	21.36 \pm 0.03	89.3 \pm 0.8	-7.3 \pm 0.4	-10.1 \pm 0.2	13.4	-2.38 \pm 0.12	-	N
298.21550	-22.08104	20.65 \pm 0.01	20.00 \pm 0.01	21.36 \pm 0.03	-177.4 \pm 1.0	-1.4 \pm 1.0	-1.2 \pm 0.6	12.1	-2.60 \pm 0.12	-	Y
298.14837	-22.04551	20.64 \pm 0.01	19.99 \pm 0.01	21.26 \pm 0.03	-176.7 \pm 1.3	1.0 \pm 1.3	0.6 \pm 0.7	12.6	-99.0 \pm 0.00	-	Y
298.13415	-22.04367	21.03 \pm 0.01	20.46 \pm 0.01	21.58 \pm 0.04	-267.1 \pm 2.5	-1.0 \pm 1.5	-2.2 \pm 0.9	5.3	-2.99 \pm 0.12	-	N
298.11950	-22.02553	21.19 \pm 0.01	20.56 \pm 0.01	21.89 \pm 0.05	-279.0 \pm 2.8	-2.0 \pm 2.4	-7.7 \pm 1.4	6.7	-2.44 \pm 0.12	-	N

Table 1 – continued

RA (deg)	DEC (deg)	g_0	i_0	$CaHK_0$	v_r (km s ⁻¹)	μ_a^* (mas yr ⁻¹)	μ_δ (mas yr ⁻¹)	S/N	[Fe/H] _{CaHK}	[Fe/H] _{spectro} ^{S10}	Member
298.14955	-22.10703	21.24 ± 0.01	20.62 ± 0.01	21.89 ± 0.05	-174.5 ± 11.9	4.8 ± 3.1	2.9 ± 1.8	3.4	-2.69 ± 0.12	-	Y
298.03665	-22.04132	18.13 ± 0.01	17.23 ± 0.01	19.54 ± 0.01	127.2 ± 0.5	0.2 ± 3.5	-1.4 ± 1.8	105.2	-1.23 ± 0.12	-1.19 ± 0.17	N
298.09544	-22.14968	19.71 ± 0.01	18.89 ± 0.01	20.98 ± 0.02	-2.7 ± 0.9	0.1 ± 1.4	-1.9 ± 0.7	31.0	-1.25 ± 0.12	-1.36 ± 0.15	N
298.06312	-22.11093	20.13 ± 0.01	19.44 ± 0.01	21.05 ± 0.02	-29.5 ± 1.1	-0.3 ± 0.8	-1.3 ± 0.4	12.8	-99.0 ± 0.00	-1.37 ± 0.17	N
298.05710	-22.02942	20.59 ± 0.01	20.02 ± 0.01	21.35 ± 0.03	-63.9 ± 0.8	2.7 ± 1.8	0.4 ± 1.0	10.9	-1.89 ± 0.12	-	N
297.96338	-22.04654	20.35 ± 0.01	19.76 ± 0.01	21.11 ± 0.02	-18.8 ± 1.5	- ± -	- ± -	12.1	-1.99 ± 0.12	-1.61 ± 0.16	N
298.15344	-22.04959	17.76 ± 0.01	16.74 ± 0.01	18.98 ± 0.01	-175.5 ± 0.3	-0.9 ± 0.4	-1.0 ± 0.2	125.2	-2.31 ± 0.12	-2.23 ± 0.12	Y
298.28018	-22.12346	17.18 ± 0.01	16.40 ± 0.01	18.60 ± 0.01	-14.2 ± 0.4	-0.3 ± 1.3	0.8 ± 0.8	131.5	-	-1.19 ± 0.18	N
298.01474	-21.91537	17.29 ± 0.01	16.29 ± 0.01	18.90 ± 0.01	-48.0 ± 0.4	-4.0 ± 1.7	-8.8 ± 1.0	131.5	-	-1.23 ± 0.18	N

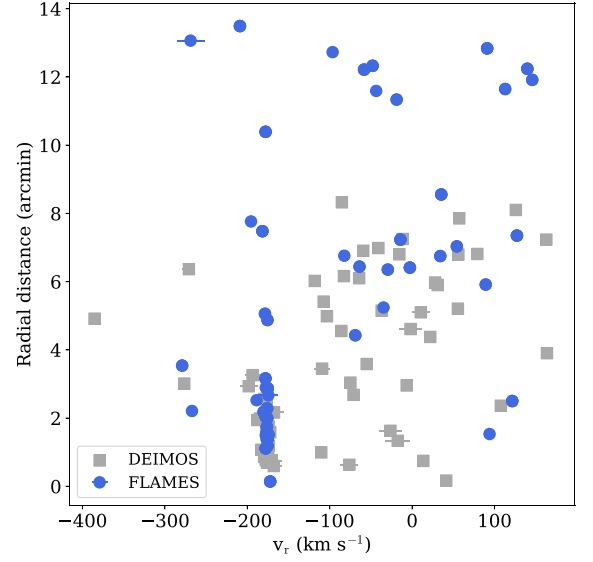


Figure 4. Heliocentric velocities versus radial distance to Sgr II's centroid for FLAMES (blue circles) and DEIMOS (grey squares) data sets. The addition of the FLAMES data doubles the number of identified members for Sgr II. All error bars not appearing in this plot are smaller than the size of the circles/squares.

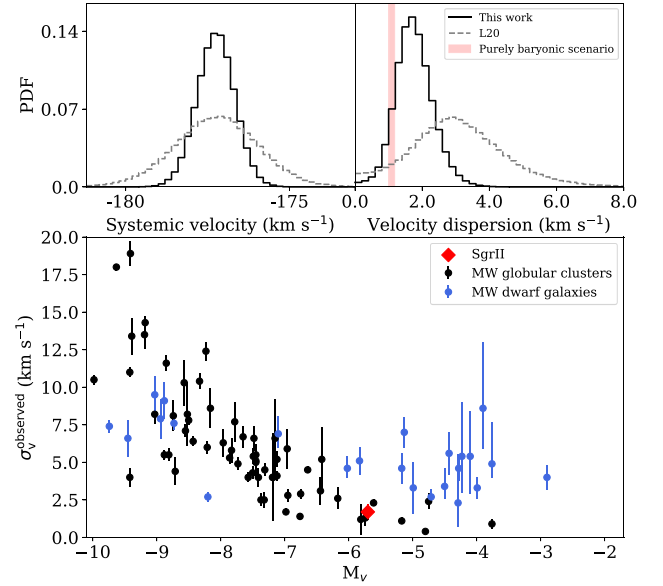


Figure 5. 1D marginalized PDFs of the systemic radial velocity (top left-hand panel) and velocity dispersion (top right-hand panel) of Sgr II from this work as black solid lines, and L20 in grey dashed lines using only DEIMOS data. The expected velocity dispersion for a Sgr II-like typical MW globular cluster (1.1 ± 0.1 km s⁻¹) is indicated as the red shaded region. The bottom panel shows the observed velocity dispersions of most globular clusters (black) and confirmed dwarf galaxies (blue) of the MW as a function of their absolute magnitudes. The properties of the globular clusters were taken from the Harris (2010) catalogue and references therein. The dwarf galaxy measurements come from Simon (2019) and references therein. In this plot, the location of Sgr II is indicated by the red diamond.

region of the satellite and is therefore more likely to find Sgr II stars, while the FLAMES observations had a much wider field of view and aim to find stars located much further away than Sgr II's centroid.

4 RESULTS: METALLICITY PROPERTIES

In the following section, the mean stellar metallicity of Sgr II and its metallicity dispersion are derived using our new FLAMES data. To do so, we select only non-binary, non-HB stars with a spectral signal-to-noise ratio greater than 12 and with $g_0 < 20.5$ (i.e. ~ 1 mag below the HB of Sgr II). These quality criteria are applied to ensure that the spectra in the region of the Calcium triplet lines are of good enough quality to be able to confidently apply the empirical relation of Starkenburg et al. (2010) and to restrict ourselves to red giant branch (RGB) stars only. This yields a subsample of 17 stars to extract a measurement of the spectroscopic metallicity. This procedure is performed through the use of the empirical calibration of Starkenburg et al. (2010) that uses the equivalent widths (EWs) of the Calcium II triplet lines to deduce a measurement of the metallicity of a star. The uncertainties on the coefficients defining the polynomials to transform a set of EWs into a $[\text{Fe}/\text{H}]_{\text{spectro}}$ are folded in with the uncertainties on the EWs through a Monte Carlo procedure. For each star, the spectroscopic metallicity is computed 2000 times by randomly drawing an EW measurement as well as randomly drawing the coefficients assuming that all these uncertainties follow a Gaussian behaviour. Since the relation of Starkenburg et al. (2010) relies on absolute magnitudes, the uncertainty on the distance modulus of the satellite as derived by L20 is also taken into account. This procedure yields a spectroscopic metallicity PDF for each star, that enables us to compute the favoured metallicity value as well as its uncertainty for each star. We take the value of 8 per cent reported by Starkenburg et al. (2010) to be the uncertainty on each coefficient. We note that these uncertainties do not include several systematics (due to, for instance, the continuum placement, or the detailed chemical abundance pattern of the star when transforming a Ca II measurement into $[\text{Fe}/\text{H}]$). Fig. 6 shows the spectroscopic metallicities of the 17 stars and their uncertainties assuming each measurement can be modelled by a Gaussian centred on $[\text{Fe}/\text{H}]_{\text{spectro}}$ and with a standard deviation corresponding to $\delta_{[\text{Fe}/\text{H}]}$. For stars observed more than once, a metallicity measurement is derived for each epoch and we verify that each epoch yields a metallicity compatible with the others. This procedure highlights two stars with a discrepant metallicity measurement for one of the three epochs during which they were observed. This epoch is the same for both stars. After a careful examination of the spectra, we conclude that the measurements at this epoch for the two stars suffer for a very low S/N ratio around the Calcium triplet spectral region ($S/N \sim 6$), which is not the case for the two other epochs. This is likely to be the source of the discrepant metallicity between the different epochs for these two stars. In order to be conservative, we decide to discard those stars for the rest of the analysis. However, including those stars in the sample by only considering the epochs when the S/N ratios is sufficient strengthens the conclusion of the analysis. None of the four stars in common between the FLAMES and DEIMOS samples have a spectroscopic metallicity measurement.

Since all 15 stars in the subsample are likely Sgr II members, their metallicity distribution is assumed to be only reflective of Sgr II population, which is therefore modelled with a Gaussian distribution weighted with the membership probability of each star according to L20. We find a spectroscopic systemic metallicity of $\langle [\text{Fe}/\text{H}]_{\text{spectro}}^{\text{SgrII}} \rangle = -2.23 \pm 0.06$, and an unresolved metallicity

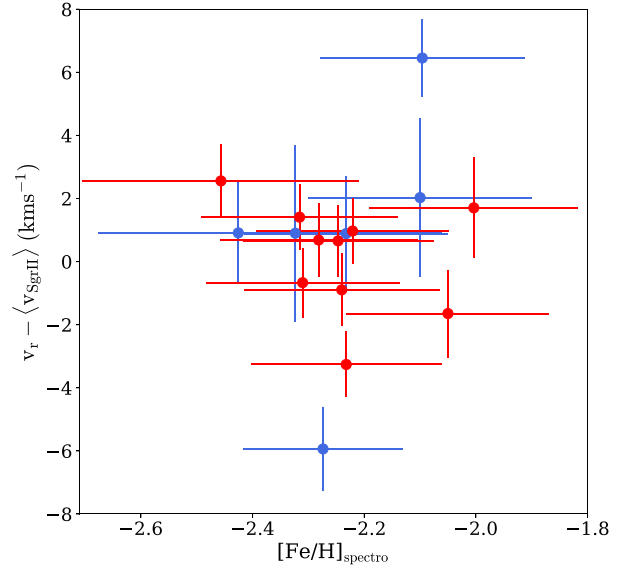


Figure 6. Individual metallicities of all bright stars in the spectroscopic sample used to derive the metallicity properties of Sgr II using the calibration of Starkenburg et al. (2010). Each measurement is modelled by a Gaussian with a mean corresponding to the favoured metallicity of the star, and a standard deviation equal to its uncertainty. Stars from the L20 sample are shown as blue dots, while the new FLAMES stars are represented in red.

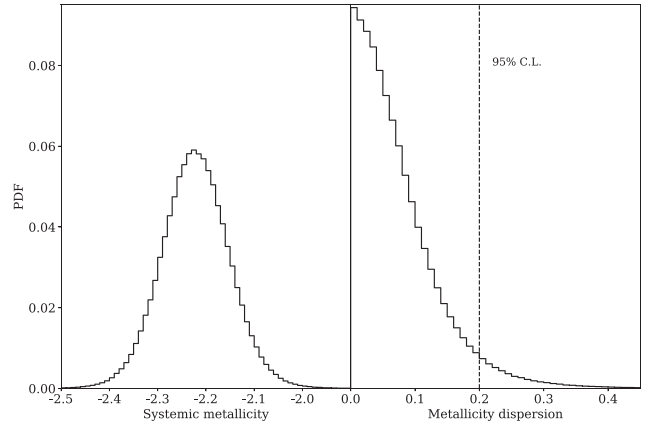


Figure 7. 1D PDFs of the systemic metallicity (left-hand panel) and metallicity dispersion (right-hand panel) of Sgr II with spectroscopy. The 95 per cent C.L. on the metallicity dispersion is shown as a black dashed line.

dispersion with $\sigma_{\text{spectro}}^{\text{SgrII}} < 0.20$ at the 95 per cent confidence limit. The PDFs corresponding to these results are shown in Fig. 7. The metallicity dispersion is unresolved, and is constrained to be below 0.20 dex at the 95 per cent confidence limit (C.L.). Including the two stars with one discrepant metallicity measurement among the three epochs, as mentioned in the previous paragraph, tightens this constrain with a metallicity dispersion that is below 0.13 dex at the 95 per cent C.L..

5 DISCUSSION

Throughout this paper, we analyse the dynamical and metallicity properties of the faint MW satellite Sgr II. To this end, we combine the Keck II/DEIMOS spectroscopic data set of our previous analysis

of the satellite with new VLT/FLAMES data. These FLAMES observations are the first ones to be carried out by selecting a priori the interesting candidates using the narrow-band, metallicity sensitive photometry of the Pristine survey for a faint satellite of the MW. The spectroscopic observations presented in this work are decisive as they double the overall sample of members stars known. Nine new stars are bright enough to estimate their spectroscopic metallicities with the empirical Calcium II triplet calibration of Starkenburg et al. (2010), while the sample of L20 only consists of six stars. Therefore, this study considerably enlarges the statistics available for the satellite and allows us to put much improved constraints on the dynamical and metallicity properties of Sgr II.

The systemic radial velocity of Sgr II is found to be $\langle v_{\text{SgrII}} \rangle = -177.2^{+0.5}_{-0.6} \text{ km s}^{-1}$. The velocity dispersion of $\sigma_{v_{\text{SgrII}}} = 1.7 \pm 0.5 \text{ km s}^{-1}$ is well among the range observed for the MW globular clusters at the same luminosity, as shown in Fig. 5. It translates into an M/L ratio of $3.5^{+2.7}_{-1.6} M_{\odot} L_{\odot}^{-1}$, thus suggesting that the dynamics of the satellite is not mainly driven by a DM halo. We identify 19 new members in the faint system, for a total of 43 confirmed spectroscopic Sgr II members. With a fraction of member identified over the entirety of the FLAMES sample of 60 per cent, the a priori selection using Pristine performs three times better than the simple CMD-based selection of L20, despite a riskier observational strategy through the search for stars located beyond two half-light radii of the satellite. Four of these stars are identified, with the outermost one lying at $6.2r_h$. Given the distance of this star, the tidal radius of Sgr II is estimated assuming a King profile and is found to be of ~ 10 half-light radii. Therefore, we do not claim that this star has been tidally stripped. Out of the 43 members, 15 have good enough quality spectra to measure the EWs of their Calcium II triplet and measure their metallicity using the empirical calibration of Starkenburg et al. (2010). We find a systemic metallicity of -2.23 ± 0.07 and constrain the metallicity dispersion of the satellite to be less than 0.20 at the 95 per cent confidence limit.

The velocity dispersion as inferred by L20 is larger than the one found in the present analysis. Furthermore, L20's metallicity analysis indicates that there are multiple stellar populations in the system, as the metallicity dispersion is resolved both with CaHK photometry and spectroscopy. Moreover, two stars in the small-sized sample of 6 with a [Fe/H] measurement in L20 have discrepant metallicity measurements. This is not the case anymore in this work as the spectroscopic metallicity distribution of our data set is well-described with only one stellar population despite the addition of nine new stars with spectroscopic metallicities. Moreover, Fig. 6 shows that no star with a metallicity below -2.5 is confidently detected, a limit commonly attributed to the lowest metallicity achievable by globular clusters (Harris 2010 and references therein, Beasley et al. 2019). Therefore, we are able to conclude that Sgr II is a globular cluster.

None the less, the satellite is still quite extended when compared to other MW globular clusters of the same luminosity. Within a range of one magnitude around Sgr II's absolute magnitude, the largest MW cluster is Pal 5 ($M_V \sim -5.2$), a fairly metal-poor system ([Fe/H] ~ -1.4) with a size of $\sim 19.2 \text{ pc}$, while most of the others have a size below 10 pc (Harris 2010). Whether we consider the distance of L20 or Vivas, Martínez-Vázquez & Walker (2020), Sgr II is still at least 1.5 times more extended than Pal 5. Sgr II is a case in point of the ambiguity surrounding the faint MW satellites discovered in recent years, with a somewhat larger half-light radius than expected from GCs at that luminosity, a metallicity perfectly compatible with the luminosity–metallicity relation of dwarf galaxies (Kirby et al. 2013b), and velocity and metallicity dispersions challenging to resolve. Though we conclude that Sgr II is an old and metal-poor

globular cluster, the system remains interesting in many aspects, from its possible association to the Sgr stream to an even deeper understanding of the unusually large cluster, which could build a bridge to the still exclusive definitions of clusters and galaxies of the MW.

ACKNOWLEDGEMENTS

We thank the anonymous referee for the very detailed and useful reports that undoubtedly improved the quality of the paper.

We gratefully thank the Canada-France-Hawaii Telescope staff for performing the observations in queue mode, for their reactivity in adapting the schedule, and for answering our questions during the data-reduction process.

NFM, RI, and NL gratefully acknowledge support from the French National Research Agency (ANR) funded project ‘Pristine’ (ANR-18-CE31-0017) along with funding from CNRS/INSU through the Programme National Galaxies et Cosmologie and through the CNRS grant PICS07708. ES gratefully acknowledges funding by the Emmy Noether program from the Deutsche Forschungsgemeinschaft (DFG). This work has been published under the framework of the IdEx Unistra and benefits from a funding from the state managed by the French National Research Agency as part of the investments for the future program. The authors thank the International Space Science Institute, Berne, Switzerland for providing financial support and meeting facilities to the international team ‘Pristine’.

Based on observations collected at the European Southern Observatory under ESO programme(s) 099.B-0690(A).

Some of the data presented herein were obtained at the W. M. Keck Observatory, which is operated as a scientific partnership among the California Institute of Technology, the University of California, and the National Aeronautics and Space Administration. The Observatory was made possible by the generous financial support of the W. M. Keck Foundation. Furthermore, the authors wish to recognize and acknowledge the very significant cultural role and reverence that the summit of Maunakea has always had within the indigenous Hawaiian community. We are most fortunate to have the opportunity to conduct observations from this mountain.

Based on observations obtained at the Canada–France–Hawaii Telescope which is operated by the National Research Council of Canada, the Institut National des Sciences de l’Univers of the Centre National de la Recherche Scientifique of France, and the University of Hawaii.

This work has made use of data from the European Space Agency (ESA) mission *Gaia* (<https://www.cosmos.esa.int/gaia>), processed by the *Gaia* Data Processing and Analysis Consortium (DPAC, <https://www.cosmos.esa.int/web/gaia/dpac/consortium>). Funding for the DPAC has been provided by national institutions, in particular the institutions participating in the *Gaia* Multilateral Agreement.

DATA AVAILABILITY

The data underlying this article are available in the article.

REFERENCES

- Aguado D. S. et al., 2019, *MNRAS*, 490, 2241
- Beasley M. A., Baugh C. M., Forbes D. A., Sharples R. M., Frenk C. S., 2002, *MNRAS*, 333, 383
- Beasley M. A., Trujillo I., Leaman R., Montes M., 2018, *Nature*, 555, 483
- Beasley M. A., Leaman R., Gallart C., Larsen S. S., Battaglia G., Monelli M., Pedreros M. H., 2019, *MNRAS*, 487, 1986

- Belokurov V. et al., 2006, *ApJ*, 647, L111
- Blakeslee J. P., 1997, *ApJ*, 481, L59
- Brodie J. P., Huchra J. P., 1991, *ApJ*, 379, 157
- Bullock J. S., Boylan-Kolchin M., 2017, *ARA&A*, 55, 343
- Carretta E., Bragaglia A., Gratton R., D'Orazi V., Lucatello S., 2009, *A&A*, 508, 695
- Chantereau W., Charbonnel C., Meynet G., 2016, *A&A*, 592, A111
- Cohen J. G., Kirby E. N., Simon J. D., Geha M., 2010, *ApJ*, 725, 288
- Côté P., Djorgovski S. G., Meylan G., Castro S., McCarthy J. K., 2002, *ApJ*, 574, 783
- Côté P., West M. J., Marzke R. O., 2002, *ApJ*, 567, 853
- Dekel A., Silk J., 1986, *ApJ*, 303, 39
- Drlica-Wagner A. et al., 2015, *ApJ*, 813, 109
- Faber S. M. et al., 2003, *Proc. SPIE*, 4841, 1657
- Frebel A., Norris J. E., 2015, *ARA&A*, 53, 631
- Fritz T. K., Carrera R., Battaglia G., Taibi S., 2019, *A&A*, 623, A129
- Gaia Collaboration, 2018, *A&A*, 616, A1
- Geringer-Sameth A., Koushiappas S. M., Walker M., 2015, *ApJ*, 801, 74
- Gieles M. et al., 2018, *MNRAS*, 478, 2461
- Gilmore G., Wilkinson M. I., Wyse R. F. G., Kleya J. T., Koch A., Evans N. W., Grebel E. K., 2007, *ApJ*, 663, 948
- Gratton R. G. et al., 2007, *A&A*, 464, 953
- Gratton R., Bragaglia A., Carretta E., D'Orazi V., Lucatello S., Sollima A., 2019, *A&AR*, 27, 8
- Harris W. E., 2010, preprint ([arXiv:1012.3224](https://arxiv.org/abs/1012.3224))
- Hastings W. K., 1970, *Biometrika*, 57, 97
- Homma D. et al., 2016, *ApJ*, 832, 21
- Homma D. et al., 2019, *PASJ*, 71, 94
- Ishiyama T., Sudo K., Yokoi S., Hasegawa K., Tominaga N., Susa H., 2016, *ApJ*, 826, 9
- Ivezić Ž. et al., 2008, *ApJ*, 684, 287
- Jethwa P., Erkal D., Belokurov V., 2018, *MNRAS*, 473, 2060
- Ji A. P., Simon J. D., Frebel A., Venn K. A., Hansen T. T., 2019, *ApJ*, 870, 83
- Kim D., Jerjen H., 2015, *ApJ*, 799, 73
- Kirby E. N., Simon J. D., Geha M., Guhathakurta P., Frebel A., 2008, *ApJ*, 685, L43
- Kirby E. N., Boylan-Kolchin M., Cohen J. G., Geha M., Bullock J. S., Kaplinghat M., 2013a, *ApJ*, 770, 16
- Kirby E. N., Cohen J. G., Guhathakurta P., Cheng L., Bullock J. S., Gallazzi A., 2013b, *ApJ*, 779, 102
- Kleya J. T., Wilkinson M. I., Evans N. W., Gilmore G., 2005, *ApJ*, 630, L141
- Klypin A., Kravtsov A. V., Valenzuela O., Prada F., 1999, *ApJ*, 522, 82
- Koposov S. E. et al., 2011, *ApJ*, 736, 146
- Koposov S. E. et al., 2015, *ApJ*, 811, 62
- Koposov S. E., Belokurov V., Torrealba G., 2017, *MNRAS*, 470, 2702
- Laevens B. P. M. et al., 2015, *ApJ*, 813, 44
- Longeard N. et al., 2018, *MNRAS*, 480, 2609
- Longeard N. et al., 2020, *MNRAS*, 491, 356
- Martin N. F., Jin S., 2010, *ApJ*, 721, 1333
- Martin N. F., Ibata R. A., Chapman S. C., Irwin M., Lewis G. F., 2007, *MNRAS*, 380, 281
- Martin N. F. et al., 2016a, *MNRAS*, 458, L59
- Martin N. F. et al., 2016b, *ApJ*, 818, 40
- Martin N. F. et al., 2016c, *ApJ*, 830, L10
- Massari D., Helmi A., 2018, *A&A*, 620, A155
- Mau S. et al., 2019, *ApJ*, 875, 154
- Melo C., Primas F., Pasquini L., Patat F., Smoker J., 2009, *Messenger*, 135, 17
- Mo H., van den Bosch F. C., White S., 2010, *Galaxy Formation and Evolution*. Cambridge Univ. Press, Cambridge
- Moore B., 1996, *ApJ*, 461, L13
- Nadler E. O., Gluscevic V., Boddy K. K., Wechsler R. H., 2019, *ApJ*, 878, L32
- Pasquini L. et al., 2002, *Messenger*, 110, 1
- Pfeffer J., Kruijssen J. M. D., Crain R. A., Bastian N., 2018, *MNRAS*, 475, 4309
- Riley A. H., Strigari L. E., 2020, *MNRAS*, 494, 983
- Roederer I. U. et al., 2016, *AJ*, 151, 82
- Schaye J. et al., 2015, *MNRAS*, 446, 521
- Shapley H., 1938a, *Harvard Coll. Obs. Bull.*, 908, 1
- Shapley H., 1938b, *Nature*, 142, 715
- Simon J. D., 2019, *ARA&A*, 57, 375
- Simon J. D., Geha M., 2007a, *ApJ*, 670, 313
- Simon J. D., Geha M., 2007b, *ApJ*, 670, 313
- Simon J. D. et al., 2011, *ApJ*, 733, 46
- Simon J. D. et al., 2017, *ApJ*, 838, 11
- Simon J. D. et al., 2020, *ApJ*, 892, 137
- Simon J., Fu S. W., Geha M., Kelson D. D., Alarcon Jara A. G., 2019, *American Astronomical Society Meeting Abstracts*, Vol. 233, American Astronomical Society Meeting Abstracts #233. 449.04
- Springel V. et al., 2008, *MNRAS*, 391, 1685
- Starkenburg E. et al., 2010, *A&A*, 513, A34
- Starkenburg E. et al., 2017, *MNRAS*, 471, 2587
- Torrealba G. et al., 2018, *MNRAS*, 475, 5085
- Villaume A., Romanowsky A. J., Brodie J., Strader J., 2019, *ApJ*, 879, 45
- Vivas A. K., Martínez-Vázquez C., Walker A., 2020, *ApJS*, 247, 35
- Vogelsberger M. et al., 2014, *MNRAS*, 444, 1518
- Walker M. G. et al., 2016, *ApJ*, 819, 53
- Webster D., Frebel A., Bland-Hawthorn J., 2016, *ApJ*, 818, 80
- Wheeler C. et al., 2019, *MNRAS*, 490, 4447
- White S. D. M., Rees M. J., 1978, *MNRAS*, 183, 341
- Willman B., Strader J., 2012, *AJ*, 144, 76
- Willman B. et al., 2005, *ApJ*, 626, L85
- Wolf J., Martinez G. D., Bullock J. S., Kaplinghat M., Geha M., Muñoz R., Simon J. D., Avedo F. F., 2010, *MNRAS*, 406, 1220
- Youakim K. et al., 2017, *MNRAS*, 472, 2963
- Zucker D. B. et al., 2006, *ApJ*, 650, L41

This paper has been typeset from a \LaTeX file prepared by the author.